

# Spectral Interferometric Microscopy for Fast and Broadband Phase Characterization

Lior Michaeli,<sup>\*</sup> Danielle Ben Haim, Mukesh Sharma, Haim Suchowski, and Tal Ellenbogen

The rapid growth in the development of new optical materials such as 2D materials, layered heterostructures, active phase changing materials, optical metasurfaces, and metamaterials, requires new methods which enable accurate, broadband, and real-time microscopic characterization of their optical and physical properties. Here, this necessity is addressed and a novel method is presented to dynamically and accurately obtain the spectral phase of a microscopic sample, either in reflection or transmission. The method is based on a designed optical relay that couples the output port of a typical microscope setup to an imaging spectrometer. By post-processing the acquired images, a stable, accurate, and easy-to-align broadband spectral microscopic interferometer is obtained. This approach is experimentally demonstrated by measuring the spectral phase response of two different types of metasurfaces in reflection and in transmission and also by accurately measuring the dispersion of a thick glass slab in transmission. Moreover, the method's applicability to broadband dynamic measurements is demonstrated by real-time tracking the phase response of optically driven nematic to isotropic and isotropic to nematic phase transitions of a liquid crystal. Altogether this method enables accurate, dynamic, and easy microscopic phase characterization and can become widely used for materials characterization.

characterization of the sample's optical and physical properties. For example, it enables detection and quantification of exotic phenomena such as negative refraction,<sup>[1–5]</sup> artificial magnetism,<sup>[6–10]</sup> zero refractive index,<sup>[11–13]</sup> and electromagnetic-induced transparency (EIT) behavior and its associated slow light.<sup>[14–16]</sup> Numerous optical schemes exist for direct broadband interferometric phase measurements. Typically they rely on recording either the time-resolved interferogram (TRI)<sup>[17,18]</sup> or spectrally resolved interferogram (SRI)<sup>[17,19]</sup> of two interfering light beams. Obtaining the interferogram in these methods can either be done by successive acquisitions, e.g., with the use of a delay stage for TRI or tunable source for SRI, or by simultaneous acquisition where the entire interferogram is obtained in a single shot. For SRI, such simultaneous acquisition merely requires a spectrometer, whereas a more sophisticated method is required for the case of TRI. For example, by mapping the relative delay of the two interfering beams into different spatial positions in an off-axis con-

figuration, and simultaneously recording the intensity with a detector array. In this approach, the spatially resolved interferogram (SRI) is obtained, which is directly mapped into the TRI.

In addition to these widely used methods, the quest for simpler experimental technique, with better spectral resolution and shorter acquisition times, mainly driven by the need for characterization of ultra-short pulses has resulted in development of a new class of interferometers: spatially and spectrally resolved interferometers (SSRIs).<sup>[20–23]</sup> In this class, a camera is used to record the interference pattern of two beams in an off-axis configuration, where one axis is devoted to the spatial resolution and the other, by the aid of a diffraction grating, to spectral resolution. These methods, which enable single-shot broadband spectral phase extraction without any moving mechanical parts, have been demonstrated adequate for challenging pulse characterization<sup>[24–26]</sup> and have also been improved to show better temporal<sup>[27]</sup> or spatial<sup>[28]</sup> capabilities. Detailed review and analysis of these methods can be found in Borzsonyi et al.<sup>[29,30]</sup>

The integration of the appealing SSRI technique with optical microscopy has been suggested by O'Brien et al.,<sup>[31]</sup> where based on Mach–Zehnder reflective interferometer

## 1. Introduction

Measuring the spectral phase of light reflected or transmitted from a microscopic sample is often required for the full

L. Michaeli, D. Ben Haim, Dr. M. Sharma, Prof. T. Ellenbogen  
Department of Physical Electronics  
Faculty of Engineering  
Tel-Aviv University  
Tel-Aviv 6779801, Israel  
E-mail: liormic1@mail.tau.ac.il

L. Michaeli, Prof. H. Suchowski  
Raymond and Beverly Sackler School of Physics & Astronomy  
Tel-Aviv University  
Tel-Aviv 6779801, Israel

L. Michaeli, D. Ben Haim, Dr. M. Sharma, Prof. H. Suchowski,  
Prof. T. Ellenbogen  
Center for Light-Matter Interaction  
Tel-Aviv University  
Tel-Aviv 6779801, Israel

 The ORCID identification number(s) for the author(s) of this article can be found under <https://doi.org/10.1002/adom.202000326>.

DOI: 10.1002/adom.202000326

they have successfully demonstrated phase characterization of metasurface sustaining plasmonic EIT. One of the challenges in merging microscopy, spectroscopy, and interferometry lies in the dispersive nature of the optics used for the imaging and magnification in addition to the microscope slide, which typically set much larger spectral phase variations to the sample beam than the sample itself. In addition, the difficulty of realizing broadband single-shot phase acquisition of microscopic samples in a common-path configuration sets severe limits on the complexity of such optical setups and on their sensitivity to noise. Gennaro et al. have reported such a configuration, based on SSRI integrated within a microscope, where they successfully realized a common-path configuration, by the use of two objective lenses, for the illumination and collection of light from the sample.<sup>[32]</sup> Very recently, a technique using similar concepts, though for only a single wavelength, has been reported.<sup>[33]</sup> This technique benefits from relatively stabilized time-dependent noise owing to three-beam interference. These two mentioned methods<sup>[32,33]</sup> require tightly focused illumination, and are not suitable for collimated beam illumination schemes, angle-resolved measurements, or for structured beam illumination. Thus, their use is not suited for many applications, e.g., the extraction of consecutive material effective parameters by complex S-parameters measurements,<sup>[34–36]</sup> or the characterization of phenomena as surface lattice resonances in plasmonic metasurfaces.<sup>[37,38]</sup>

Here, we present a novel approach to overcome these limitations, by implementing an SSRI in a common-path configuration based on a double-hole mask located at the image plane of the microscope. The novel Masked Image-plane Common-path self-Referenced Optical SSRI (MICRO-SSRI) enables flexible sample illumination, stable, accurate, and easy-to-align single-acquisition spectral phase extraction by only slightly modifying a typical spectroscopy microscope setup. We experimentally demonstrate this powerful method by performing a set of challenging phase measurements, which require the following capabilities: microscopic resolution, plane wave illumination, transmission and reflection modes, large dynamic range of phase change (much bigger than  $2\pi$ ), and real-time dynamic characterization. Specifically, our experimental demonstrations include measurements in transmission mode of 170  $\mu\text{m}$  thick glass, which enable extraction of the wavelength-dependent refractive index, and also serve as a spectral phase target for the demonstration of the methods accuracy. Furthermore, to show the applicability of the method to characterize new materials, we also measure the phase response of a plasmonic metasurface sustaining an angle-dependent EIT behavior, and the rich spectral phase response in reflection of a reflective Fabry–Perot metasurface-based element. The experimental results are in good agreement to finite-difference-time-domain (FDTD) simulation results. In addition, to examine the applicability of the method for examination of time varying systems, we performed real-time dynamic broadband phase measurements of a nematic liquid crystal (LC) under optically induced conformation. We identify in our measurements both continuous phase changes, associated with the temperature-

dependent refractive index of the LC, and discontinuities associated with the abrupt change in the order parameter at the isotropic–nematic and nematic–isotropic phase transitions. Finally, we also discuss how further manipulating the image plane of the microscope enables even more accurate and stabilized measurements in only a single shot, based on three-beam interference.

## 2. Setup Description

In this section, we describe the working principle of our phase measurement technique. **Figure 1a** shows the schematic illustration of the configuration used for the phase characterization. Incoming broadband light is shined on the plane containing the sample and the reference areas, here shown as metasurface on glass and bare glass, respectively. An objective and a tube lens are used to image and magnify the sample-reference plane. A double-hole mask located at the image plane transmits from one hole only light passing through the sample and from the other only light from the reference. A lens images the Fourier plane of the mask, which consists of two slightly angled beams from the reference and the sample, on the imaging spectrometer entrance slit to produce the broadband interferogram on the camera. **Figure 1b** shows the working principle of the two holes assisted off-axis interferometry, where the relative delay between two slightly angled light beams is mapped into different spatial positions. This occurs by the aid of the lens, transforming the light from each hole to a plane wave with well-defined angle. In the case of uncalibrated system, two acquisitions, rather than one, are required to obtain the spectral phase of the sample. These acquisitions are depicted in **Figure 1c**. In the first acquisition, the two holes,  $H_1$  and  $H_2$ , transmit light from the reference area, while in the second the double-hole mask is moved such that  $H_1$  transmits light from the reference and  $H_2$  from the sample.

According to the described scheme and the acquisitions depicted in **Figure 1c**, the two interferograms captured by the 2D-sensor array corresponds to (see full theoretical description in the Supporting Information, Section S2)

$$I_{\text{captured}}^{\text{RR}}(\lambda, \gamma) = |E_{\text{source}}^{(0)}(\lambda) T_{\text{R}}^{(0)}(\lambda)|^2 + |E_{\text{source}}^{(0)}(\lambda) T_{\text{R}}^{(0)}(\lambda)|^2 + |E_{\text{source}}^{(0)}(\lambda)|^2 |T_{\text{R}}^{(0)}(\lambda)|^2 e^{-2ik_r \gamma} + |E_{\text{source}}^{(0)}(\lambda)|^2 |T_{\text{R}}^{(0)}(\lambda)|^2 e^{2ik_r \gamma} \quad (1a)$$

$$I_{\text{captured}}^{\text{RS}}(\lambda, \gamma) = |E_{\text{source}}^{(0)}(\lambda) T_{\text{R}}^{(0)}(\lambda)|^2 + |E_{\text{source}}^{(0)}(\lambda) T_{\text{S}}^{(0)}(\lambda)|^2 + |E_{\text{source}}^{(0)}(\lambda)|^2 |T_{\text{R}}^{(0)}(\lambda)| |T_{\text{S}}^{(0)}(\lambda)| e^{i(\phi_{\text{R}}(\lambda) - \phi_{\text{S}}(\lambda))} e^{-2ik_r \gamma} + |E_{\text{source}}^{(0)}(\lambda)|^2 |T_{\text{R}}^{(0)}(\lambda)| |T_{\text{S}}^{(0)}(\lambda)| e^{-i(\phi_{\text{R}}(\lambda) - \phi_{\text{S}}(\lambda))} e^{2ik_r \gamma} \quad (1b)$$

where the sub/superscripts “R” and “S” correspond to light passing through the reference and sample areas, respectively. The light intensity  $I_{\text{captured}}(\lambda, \gamma)$  on the 2D-sensor array depends on the wavelength  $\lambda$  and spatial position  $\gamma$ , corresponding to the sensor’s horizontal and vertical axes, respectively.  $E_{\text{source}}^{(0)}(\lambda)$  is the spectral electric-field amplitude of the source, and the complex transmission amplitude of the

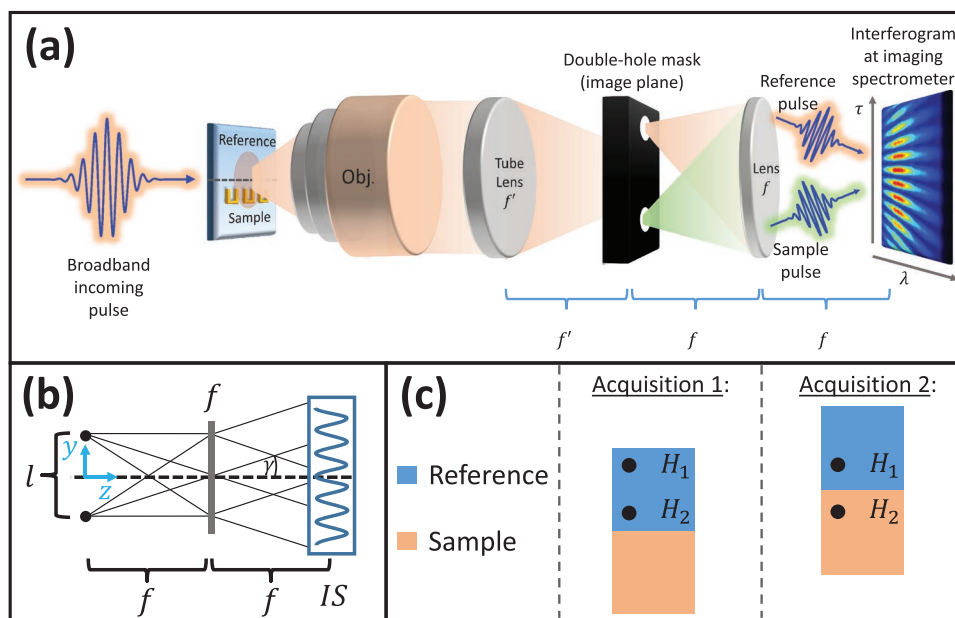


**Figure 1.** Schematic illustrations of the MICRO-SSRI working principle. a) The broadband interferogram production. Incoming broadband light is shined on the plane containing the sample and the reference, here shown as metasurface and bare glass, respectively. Double-hole mask passes from one hole only light from the sample and from the other only light from the reference. A lens images the Fourier plane of the mask on the imaging spectrometer, to produce the broadband interferogram of the sample. b) Ray optics illustration showing the slightly angled beam generation from two holes by a single lens. The distance between the holes,  $l$ , determines the half-angle between the beams  $\gamma = \tan(l/(2f))$ . c) For noncalibrated system, two acquisitions need to be taken: 1) The two holes are placed on the reference area. 2) One hole is placed on the sample and the other on the reference area.

sample/reference is divided into amplitude and phase terms according to  $T_{S,R}(\lambda) = |T_{S,R}^{(0)}(\lambda)| e^{i\phi_{S,R}(\lambda)}$ . The  $y$ -component of the wavevector  $k = 2\pi/\lambda$  is directly determined from the angle  $\gamma = \tan(l/(2f))$  by  $k_y = k \cdot \sin(\gamma)$  (see Figure 1b).

From Equation (1b), we see that the information of interest,  $\Delta\phi(\lambda) \equiv \phi_S(\lambda) - \phi_R(\lambda)$ , is encoded in the modulation at spatial frequency  $2k_y$ . To extract this phase difference, we convolve the interferograms from Equations (1) with corresponding spatial band-pass filter  $H_{BP}(\gamma)$

$$(I_{\text{captured}}^{\text{RR}}(\lambda) \odot H_{\text{BP}})(\gamma) = \pi |E_{\text{source}}^{(0)}(\lambda)|^2 |T_{\text{R}}^{(0)}(\lambda)|^2 e^{2ik_y\gamma} \quad (2a)$$

$$(I_{\text{captured}}^{\text{RS}}(\lambda) \odot H_{\text{BP}})(\gamma) = \pi |E_{\text{source}}^{(0)}(\lambda)|^2 |T_{\text{R}}^{(0)}(\lambda)| |T_{\text{S}}^{(0)}(\lambda)| e^{i\Delta\phi(\lambda)} e^{2ik_y\gamma} \quad (2b)$$

Then, by dividing Equation (2b) with Equation (2a), we get their ratio

$$r(\lambda) = \frac{|T_{\text{S}}^{(0)}(\lambda)|}{|T_{\text{R}}^{(0)}(\lambda)|} e^{i\Delta\phi(\lambda)} \quad (3)$$

The absolute value of  $r(\lambda)$  is the spectral field transmission (or reflection) and its phase is the wavelength-dependent phase difference  $\Delta\phi(\lambda)$  of interest. This way the full complex transmission or reflection spectra is obtained from only two acquisitions. For phase only information, even one acquisition is sufficient. Full setup description for both the transmission and reflection modes can be found in Section S1 of the Supporting Information.

### 3. Experimental Results

#### 3.1. Measurements of Refractive Index versus Wavelength of a Glass Slab

Here, we demonstrate the accuracy of the MICRO-SSRI method by measuring a glass slab with a specified dispersion. By accounting for the length of the sample, we extract the wavelength-dependent refractive index  $n(\lambda)$  of the glass. We show that the fine spectral resolution of the interferograms enables the obtained phase to be unambiguously unwrapped, even for a slab as thick as  $L = 170 \mu\text{m}$  as long as the refractive index is known in a single wavelength.

The measured glass slab sample was a high-performance cover slip made from Schott D263 M glass, with manufacturer reported length of  $L = 170 \pm 5 \mu\text{m}$ . **Figure 2a,b** shows the reference–reference (Figure 2a) and reference–sample (Figure 2b) interferograms (according to acquisitions 1 and 2 in Figure 1c), each obtained within a single acquisition. The large phase accumulation and dispersion of light passing through the glass sample is visually evident, in the interferogram shown in Figure 2b, by the oblique trend of the fringes. After post-processing these interferograms, as described in detail in Section S2 of the Supporting Information, we obtained the phase difference  $\Delta\phi(\lambda) = \frac{2\pi}{\lambda} \Delta n(\lambda)L$ , shown in Figure 2c. Here  $\Delta n(\lambda) \equiv n_s(\lambda) - n_r(\lambda)$  is the difference between refractive index of the sample  $n_s(\lambda)$ , and the reference (air in this case)  $n_r(\lambda) = n_{\text{air}} \approx 1$ . We note that unwarping the phase was easily done by requiring continuity of  $\Delta\phi(\lambda)$ , where the fine spectral resolution guaranteed that no phase jumps bigger

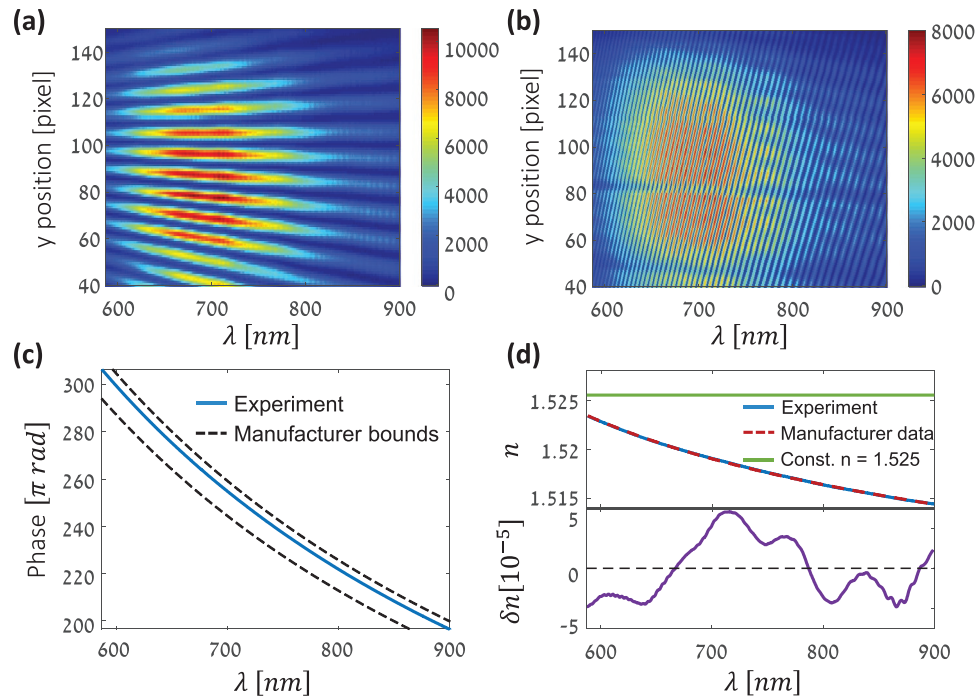


**Figure 2.** Measured interferograms of the a) reference and b) 170  $\mu\text{m}$  thick glass sample (Schott D263 M). c) The associated extracted phase of the sample is shown by the blue solid line. The black dashed lines are the manufacturer bounds for the accumulated phase. d) The top part shows the refractive index: extracted from the measurements (blue solid line), according to the manufacturer data (red dashed line) and the constant approximation of  $n = 1.525$  (green solid line). The bottom part shows the residuals according to the difference between the experimental and reported refractive index.

than  $2\pi$  were hidden in the data. We also anchored the phase in a single wavelength ( $\lambda = 666 \text{ nm}$ ) to account for the correct wrapping branch. It can be seen that phase accumulation differences of dozens of radians have been successfully recovered. By accounting for the manufacturer reported refractive index of the glass,  $n_m(\lambda)$ , and for its length,<sup>[39]</sup> we calculated the upper and lower bounds of the phase difference, shown by the black dashed lines in Figure 2c. The two bounds correspond to the 5  $\mu\text{m}$  error of the sample length. It can be seen that the measured phase is well situated between these two bounds. By isolating  $n_s(\lambda)$  from the phase expression, i.e.,  $n_s(\lambda) = n_{\text{air}} + \frac{\lambda \Delta \phi(\lambda)}{2\pi L}$ , we extracted also the sample's refractive index, shown in the top part of Figure 2d. The length used here was 172  $\mu\text{m}$ , which is in the length range of the glass. Very good agreement with the reported manufacturer data is seen, with clear deviation from the nondispersive approximation for this glass of  $n(\lambda) = 1.5255$ . The bottom part of Figure 2d shows the residuals plot according to  $\delta n(\lambda) = n_s(\lambda) - n_m(\lambda)$ . Error smaller than  $5 \times 10^{-5}$  is seen at the entire spectral range of measurements. These measurements demonstrate the accuracy of the method along with its potential to extract unambiguously the refractive index of microscopic samples. We stress that even better accuracy can be achieved by using high-end, aberration-corrected optics in an isolated optical setup.

### 3.2. Microscopic Phase Measurement of Metasurfaces

Here, we show the applicability of our technique to analysis of microscopic samples with complex phase response. For

this goal, we measure two types of metasurfaces, in reflection and in transmission. Schematic illustration of the first metasurface, that was measured in reflection, is shown in the inset of Figure 3a. The metasurface is composed of three layers: 200 nm of aluminum, 600 nm of  $\text{SiO}_2$ , and 40 nm thick squared aluminum nanodisks array of  $50 \mu\text{m} \times 50 \mu\text{m}$ . In Figure 3a, we present the broadband phase measurements of two samples: sample 1 with radius  $r = 73 \text{ nm}$  and periodicity of  $d = 270 \text{ nm}$  (blue line) and sample 2 with  $r = 48 \text{ nm}$  and  $d = 240 \text{ nm}$  (orange line). The reference used for the phase measurement is a similar structure without the nanodisks. Figure 3b shows the corresponding reflection measurements, extracted from the same acquisitions used for the phase characterization. It can be seen from the reflection that there are two dips located around  $\approx 560 \text{ nm}$  ( $\approx 540 \text{ nm}$ ) and  $\approx 780 \text{ nm}$  ( $\approx 770 \text{ nm}$ ), of the blue (orange) curves. These dips appear due to coupling of localized surface plasmon resonance (LSPR) and a Fabry–Perot mode of the structure.<sup>[40]</sup> It can be seen that the phase changes significantly around the resonance dips. At the off-resonance regimes, where the reflection is high, the phase is close to zero, as expected from the inclusions deep subwavelength depth. In Figure 3c,d, we show the phase (Figure 3c) and reflection (Figure 3d) obtained by FDTD simulations (Lumerical). For simulation details, see the Supporting Information, Section S3. The good agreement between measurements and simulation is evident.

Next, we show measurements in transmission mode of a metasurface comprised of gold split-ring resonators. The inset of Figure 4a shows a scanning electron microscope (SEM)

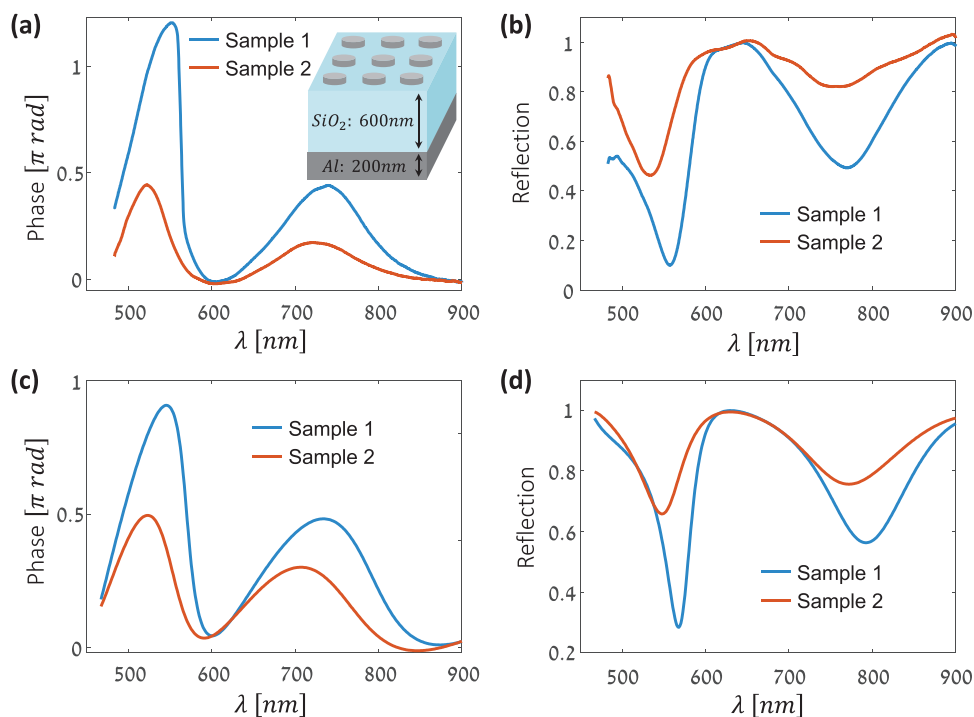


**Figure 3.** Measurements of a metasurface in reflection mode. a) Phase and b) reflection of the metasurface, for two samples with different geometrical parameters. The inset of (a) shows schematic illustration of the sample. The associated FDTD simulations of the phase and reflection are shown in (c) and (d), respectively.

image of the fabricated sample (for the sample's geometrical parameters, see the Supporting Information, Section S3). In Figure 4a, we present the broadband phase measurements for two angles of incidence:  $\theta = 0^\circ$  (blue line) and  $\theta = 30^\circ$  (orange line). Figure 4b shows the corresponding transmission measurements. It can be seen from the transmission that for normal incidence broad LSPR centered at  $\approx 840$  nm appears. The phase shows the associated phase change of the LSPR. The small phase range ( $\approx 0.2 \pi$  rad) is due to the transmitted light being a mixture of scattered light and noninteracting light. The measurements for  $\theta = 30^\circ$  show two transmission dips centered around the peak at  $\lambda \approx 906$  nm. The corresponding phase shows positive  $d\phi/d\omega$  values at the two resonances with a sharp feature at the peak location of anomalous phase, i.e., large negative  $d\phi/d\omega$  values. This phase trend reveals the existence of slow light that accompanies the high transmission value, an indication for an EIT-like behavior. These EIT-like features arise due to the interaction of the individual plasmonic particles with a lattice mode, as further described in ref. [41]. For comparison, we also simulated the phase (Figure 4c) and transmission (Figure 4d) of the measured metasurface with FDTD solver. Simulation details can be found in the Supporting Information, Section S3. Good agreement between the measurements and simulations can be seen. The deviations can originate from slight differences between simulation geometrical and materials parameters and actual ones in the experiments. The measurements and simulations of this metasurface verify that indeed our method is capable of using collimated light illumination and extract sharp spectral features spanning a small ( $<0.25 \pi$  rad) phase range.

### 3.3. Real-Time Dynamic Phase Measurements of Nematic LC under Optically Induced Conformation

In this section, we demonstrate the MICRO-SSRI method's capability to perform real-time dynamic broadband phase measurements, by tracking an optically induced nematic-isotropic LC transition. Schematic illustration of the optical configuration is shown in Figure 5a. A  $L = 12 \mu\text{m}$ , thick 4-cyano-4'-pentylbiphenyl (5CB) nematic LC layer oriented with its director horizontally, was pumped by a focused IR laser beam (1420 nm,  $\approx 140$  fs width at 80 MHz). Using two polarizers and a broadband half-wave plate mounted on a motorized rotational stage in between, the pump beam was set to be horizontally polarized and vary harmonically in intensity, as shown in Figure 5b,c, in accordance to

$$I(t) = \frac{1}{2} I_0 \left( 1 + \cos\left(2\pi \frac{t}{T}\right) \right) \quad (4)$$

where  $t$  is the time,  $I_0 = 67$  mW is the amplitude, and  $T = 45$  s is the modulation period. Due to absorption of the laser beam and consequent heating of the LC, the LC can be optically driven to change its conformation between nematic and isotropic.[42] This leads to dynamic changes in the refractive index of the LC sample, which can be used to probe the dynamic material conformation.

The dynamically changing phase of a broadband optical probe beam transmitted through the device (see Figure 5a), was measured with the interferometer, and presented in Figure 5b. The probe beam was spanning the range of 450–1000 nm, with  $\approx 2$  mm radius on the LC sample. As shown in Figure 5a, the measurements were performed such that at

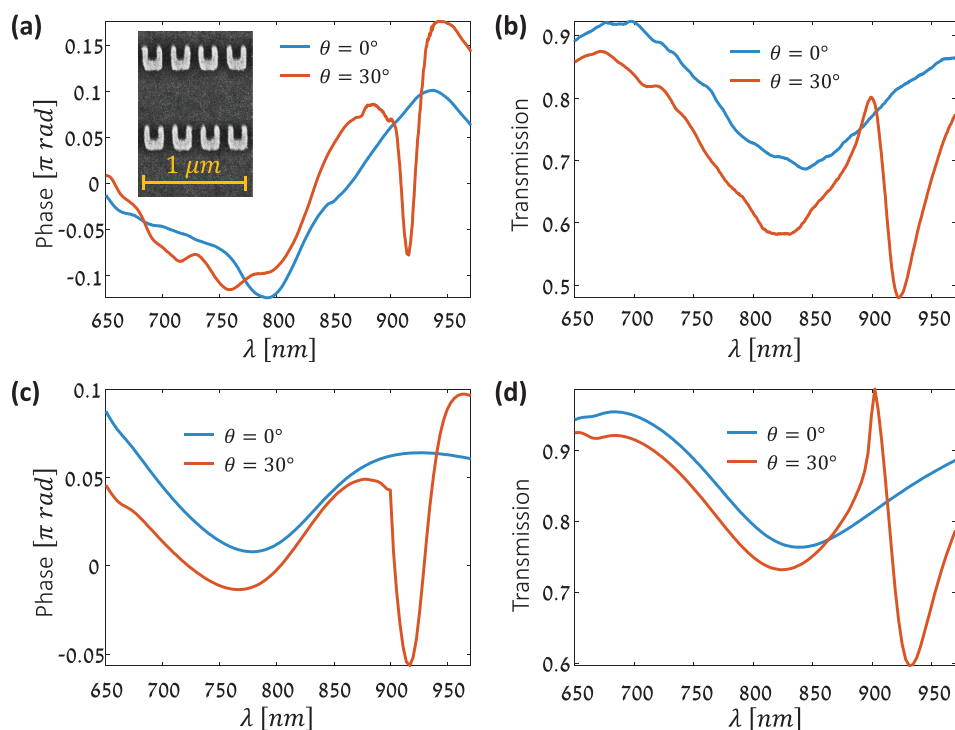


**Figure 4.** Angle-dependent measurements of a metasurface in transmission mode. The measured phase and transmission of the metasurface are shown in (a) and (b), respectively, for two angles of incidence:  $\theta = 0^\circ$  (blue line) and  $\theta = 30^\circ$  (orange line). The inset of (a) shows SEM image of the measured sample. The corresponding simulated phase and transmission are shown in (c) and (d), respectively.

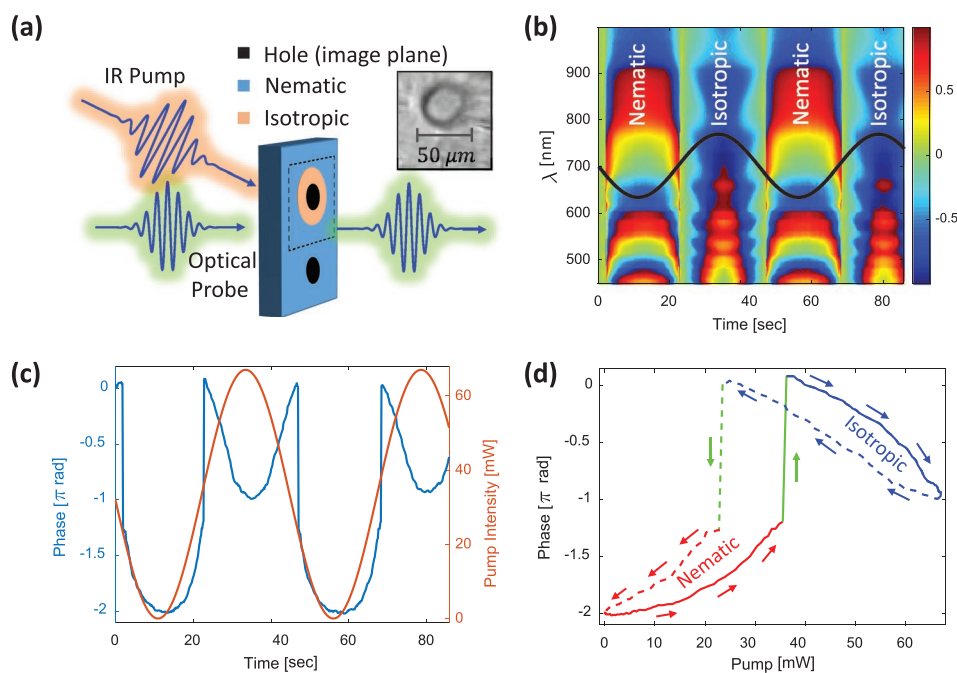


**Figure 5.** LC dynamics. a) Schematic illustration of the experimental configuration. Focused IR beam pumps the sample, and optical beam is used to probe the broadband time-resolved response. Without the pump beam, the LC is in its nematic state, while strong pump intensities can drive transitions to the isotropic state. The phase is measured at the central position of the focused pump beam. The inset shows an image of isotropic droplet formation of the LC with a circle of  $\approx 20 \mu\text{m}$  radius. b) The spectrally and temporally resolved phase response of the LC. c) Cross-section of the phase response at  $\lambda = 720 \text{ nm}$  (blue curve) and the pump intensity versus time (orange curve). d) Phase versus pump intensity of the LC for  $\lambda = 720 \text{ nm}$ . The hysteresis of the LC around the phase transitions is seen.

the image plane of the microscope, the upper hole was collecting light from the position of the incident IR beam while the lower hole was collecting light from a reference position that constantly stayed at the nematic state,  $\approx 100 \mu\text{m}$  far from the center of the pump beam. The obtained temporally resolved sequence of interferograms was post-processed such that the initial interferogram was treated as the reference interferogram. Hence, the phase map in Figure 5b shows the phase differences of the LC at the focus of the IR pump, at a given time relative to the initial phase, acquired at  $t = 0$  s. When the pump intensity reached a threshold value, the nematic LC abruptly underwent phase transition to the isotropic state. An image of the LC sample after this optically driven transition is shown in the inset of Figure 5a, where by a slightly defocused microscope image, a circle of  $\approx 20 \mu\text{m}$  radius of the isotropic state is seen. In Figure 5b, we show the raw wrapped phase, to emphasize the rich physics reflected directly from the measurements, even without the assumptions required for the unwrapping. The obtained phase values correspond to  $2\pi$ -modulus of

$$\Delta\phi(\lambda, t) = \Delta k(\lambda, t)L = \frac{2\pi}{\lambda} L(n(\lambda, t) - n^{\text{iso}}(\lambda, t=0)) \quad (5)$$

At  $t = 0$  the measured area, i.e., the area at the pump location, was at its isotropic phase, thus the reference refractive index is  $n^{\text{iso}}(\lambda, t = 0)$ . It can be seen from Figure 5b that alternating domains, each with temporal width of  $\approx 22.5$  s, exist, corresponding to the nematic and isotropic states, as marked in the figure. These domains appear in accordance with the pump intensities, qualitatively showed by the black curve. For low intensities, the LC stays at the nematic state, while for high intensities transition to the isotropic state is driven.

The phase changes versus wavelength can be easily understood. For the nematic state, the relevant index of refraction is  $n_o^{\text{nem}}(\lambda, t)$  for ordinary rays, due to the perpendicular orientation of the nematic LC director and the polarization of the probe beam. At the regions in Figure 5b corresponding to the nematic state, we see increasing phase values for increasing wavelength values. By examining Equation (5), we see that this can occur only if  $n_o^{\text{nem}}(\lambda, t) < n^{\text{iso}}(\lambda, t = 0)$ . Indeed, in accordance with the literature,<sup>[43]</sup>  $n_o^{\text{nem}}(\lambda, t)$  is smaller than  $n^{\text{iso}}(\lambda, t = 0)$  for any temperature. On the other hand, to explain the same phase trend at the isotropic state regions, we must account for the change in the temperature of the LC caused by the pump beam. If we assume that the temperature changes with proportion to the intensity of the pump beam, though with some potential time delay  $t_d$ , we can write  $T(t) = T_{\text{DC}} + T_0 \cos(2\pi f(t + t_d))$ , with  $T_{\text{DC}}$  being the DC temperature term and  $T_0$  the amplitude of the modulation. Thus, it is now evident that the coolest temperature of LC in the isotropic phase should be in vicinity to the phase transitions. Therefore, as the reference interferogram at  $t = 0$  s was taken at the isotropic state just before the isotropic-nematic transition, any further interferogram acquired in the isotropic state corresponds to higher temperature. As expected, the refractive index of the isotropic state descends with temperature.<sup>[43]</sup> Thus,  $n(\lambda, t) - n^{\text{iso}}(\lambda, t = 0) < 0$  for any interferogram of the isotropic state in the sequence, confirming the observation of the positive phase slope versus wavelength at Figure 5b. The wiggly trend accompanying the

phase versus wavelength at the isotropic states, appears due to diffraction from the circular aperture caused by the isotropic state (see inset of Figure 5a), and may be used to track the spatial evolution of the transition.

To further analyze also the temporal dependence of the phase, in Figure 5c we show a cross-section of the phase versus the time for  $\lambda = 720$  nm. The abrupt optical phase jumps that accompany the LC phase transitions are evident, while each state of the LC shows a convex trend of the optical phase. These trends can be understood by the temperature-dependent refractive index of the LC. By examining Equation (5), we see that the only time-dependent term in  $\Delta\phi(\lambda, t)$  is  $n(\lambda, t)$ . By accounting for the time-dependent temperature  $T(t)$ , for any wavelength  $\lambda$ , we obtain the relation  $\Delta\phi(\lambda, t) \propto n(\lambda, T_0 \cos(2\pi f(t + t_d)))$ . It is known from the literature<sup>[43]</sup> that  $n_o^{\text{nem}}(\lambda, T)$  and  $n^{\text{iso}}(\lambda, T)$  increase and decrease as a function of the temperature, respectively, i.e.,  $\frac{\partial n_o^{\text{nem}}(\lambda, T)}{\partial T} > 0$ , and  $\frac{\partial n^{\text{iso}}(\lambda, T)}{\partial T} < 0$ . The conclusion that arises from the last two conditions about the trend of the refractive indices and their derivatives, is that the optical phase should follow a similar trend to the pump trend, though with opposite sign for the isotropic state. This exactly agrees with the observations from Figure 5c.

Finally, in Figure 5d, we also show the measured phase versus the pump intensity, for wavelength of  $\lambda = 720$  nm. The arrows are pointing toward the direction of the device temporal evolution. The regions in red and blue correspond to the nematic and isotropic states, respectively, while the green region corresponds to the transition between these states. For any pump intensity, the phase takes one of two values, depending on the direction of the pump change, i.e., whether  $\partial I(t)/\partial t$  is positive or negative. This behavior shows the out-of-thermal-equilibrium hysteresis of the LC.

We stress here an important point regarding temporal dynamics measurements attainable with the MICRO-SSRI method. As demonstrated in this section, the method can be used for real-time characterizations. The temporal resolution of these characterizations is limited by the speed of the camera that is used, as the system has no mechanical moving parts. The limiting factor in our case was the readout rate of the imaging spectrometer's camera (Andor Newton 970), which enabled cycle time no shorter than 0.15 s. In cases where higher temporal resolution is required, one can also implement the MICRO-SSRI method within a pump-probe type experiment.<sup>[44]</sup> For this, the three-beam interference approach (see the Supporting Information, Section S4) can be particularly suited as it enables to obtain in only a single acquisition stabilized measurements.

The presented example given in this section, for real-time dynamical broadband phase characterization, shows the MICRO-SSRI method's suitability for studies concerned with temporal dynamics, highly relevant for the design of active optically controlled device applications.

#### 4. Noise and Resolution Analysis

For the static and dynamic measurements presented in this paper, there are two types of associated noise. The static measurements, used in Sections 3.1 and 3.2, rely on two successive

acquisitions (see Figure 1c), and the dynamic measurements, used in Section 3.3, are based on acquiring multiple successive interferograms and referring to the first interferogram as a reference. We refer to these two types of measurements as moving reference interferogram (MRI) and a constant reference interferogram (CRI), respectively. To estimate the temporal noise for these two types of measurements, we performed 540 successive acquisitions, equally spaced by 20 s. To calculate the standard deviation (SD) for the case of MRI, we referred to every two successive acquisitions as a couple of reference–reference and reference–sample interferograms, according to the description in Sections 2. To calculate the CRI, we refer in all measurements to the first captured frame as reference–reference interferogram. Even though the environmental conditions of the setup were not ideal including open setup and vicinity to closed-loop air-conditioning engines, we found very good SD values. For both the MRI and CRI, the SD was smaller than  $0.01 \pi$  rad. These values, influenced by various sources of vibrations, can be substantially improved by better isolations of the system. We can further improve the interferometer stability by relying on three-beam interference<sup>[33,45]</sup> within only a single acquisition (see the Supporting Information, Section S4). The method's spectral resolution is determined by the imaging spectrometer spectral resolution. In our case, it was  $\approx 0.13$  nm and can also be improved by using a system with better resolution. The spatial resolution of the method is limited by the resolution of the microscope's objective lens, often defined as  $\frac{\lambda}{2 \cdot \text{NA}}$ , where NA

is the numerical aperture. To meet this limit, the diameter of the holes at the double-hole mask should be smaller than the multiplication of the objective lens's resolution and magnification. In our implementation of the technique, the holes diameter was  $\approx 10 \mu\text{m}$ , the NA was 0.4, and the magnification was 20 and 50, for the measurements in transmission and reflection, respectively. Thus, over the entire measured range indeed the spatial resolution was determined by the objective lens.

## 5. Conclusions

We have presented the MICRO-SSRI method to obtain the spectral phase and amplitude of a microscopic sample, either in reflection or transmission. The MICRO-SSRI overcomes long standing limitations in the field of microscopy interferometry by offering a new approach of spatially filtering the collected light at the image plane of a microscope and imaging the Fourier plane of the filtered image on the entrance slit of an imaging spectrometer. This approach enables flexible sample illumination, stable and easy-to-align single, or double acquisition spectral phase extraction by only slightly modifying a typical spectroscopy microscope setup. We experimentally demonstrated the new method in measuring the phase response of metasurface samples both in reflection and transmission and showed good agreement between the simulated and measured phases. We also demonstrated the method's capability of dynamic measurements by real-time tracking the phase and amplitude of transmitted light through a nematic LC undergoing a phase transition from nematic to isotropic. Additionally, we offer a route to further decrease the noise and enhance the

interferometer stability by referring to a triple-hole mask and in only a single acquisition using the technique of three-beam interference. We believe that the MICRO-SSRI method will be useful for both microscopic and macroscopic optical material characterization. It may show special advantage for characterization of metasurfaces or 2D material. Furthermore, the opportunity to spectrally measure phase of dynamic processes with a stable and easy to align setup will be beneficial for the study of various biological, chemical, and physical processes.

## Supporting Information

Supporting Information is available from the Wiley Online Library or from the author.

## Acknowledgements

This publication is part of a project that has received funding from the European Research Council (ERC) under the European Union's Horizon 2020 research and innovation programme (grant agreement no. 715362 and grant agreement no. 639402), and by the Ministry of Science, Technology and Space, Israel (grant agreement no. 3-15614).

## Conflict of Interest

The authors declare no conflict of interest.

## Keywords

interferometers, liquid crystals, metasurfaces, optical characterization, real-time dynamics

Received: February 25, 2020

Revised: April 16, 2020

Published online:

- [1] V. M. Shalaev, W. Cai, U. K. Chettiar, H.-K. Yuan, A. K. Sarychev, V. P. Drachev, A. V. Kildishev, *Opt. Lett.* **2005**, *30*, 3356.
- [2] A. V. Kildishev, W. Cai, U. K. Chettiar, H.-K. Yuan, A. K. Sarychev, V. P. Drachev, V. M. Shalaev, *J. Opt. Soc. Am. B* **2006**, *23*, 423.
- [3] S. Zhang, W. Fan, N. C. Panoiu, K. J. Malloy, R. M. Osgood, S. R. J. Brueck, *Phys. Rev. Lett.* **2005**, *95*, 137404.
- [4] G. Dolling, C. Enkrich, M. Wegener, C. M. Soukoulis, S. Linden, *Science* **2006**, *312*, 892.
- [5] J. B. Pendry, *Phys. Rev. Lett.* **2000**, *85*, 3966.
- [6] S. Linden, C. Enkrich, G. Dolling, M. W. Klein, J. Zhou, T. Koschny, C. M. Soukoulis, S. Burger, F. Schmidt, M. Wegener, *IEEE J. Sel. Top. Quantum Electron.* **2006**, *12*, 1097.
- [7] A. I. Kuznetsov, A. E. Miroshnichenko, M. L. Brongersma, Y. S. Kivshar, B. Luk'yanchuk, *Science* **2016**, *354*, aag2472.
- [8] R. A. Shelby, D. R. Smith, S. Schultz, *Science* **2001**, *292*, 77.
- [9] J. B. Pendry, A. J. Holden, D. J. Robbins, W. J. Stewart, *IEEE Trans. Microwave Theory Tech.* **1999**, *47*, 2075.
- [10] J. Valentine, S. Zhang, T. Zentgraf, E. Ulin-Avila, D. A. Genov, G. Bartal, X. Zhang, *Nature* **2008**, *455*, 376.
- [11] P. Moitra, Y. Yang, Z. Anderson, I. I. Kravchenko, D. P. Briggs, J. Valentine, *Nat. Photonics* **2013**, *7*, 791.

- [12] R. Maas, J. Parsons, N. Engheta, A. Polman, *Nat. Photonics* **2013**, 7, 907.
- [13] H. Suchowski, K. O'Brien, Z. J. Wong, A. Salandrino, X. Yin, X. Zhang, *Science* **2013**, 342, 1223.
- [14] N. Liu, L. Langguth, T. Weiss, J. Kästel, M. Fleischhauer, T. Pfau, H. Giessen, *Nat. Mater.* **2009**, 8, 758.
- [15] S. Zhang, D. A. Genov, Y. Wang, M. Liu, X. Zhang, *Phys. Rev. Lett.* **2008**, 101, 47401.
- [16] Y. Yang, I. I. Kravchenko, D. P. Briggs, J. Valentine, *Nat. Commun.* **2014**, 5, 5753.
- [17] L. Lepetit, G. Chériaux, M. Joffre, *J. Opt. Soc. Am. B* **1995**, 12, 2467.
- [18] M. A. van Dijk, M. Lippitz, M. Orrit, *Phys. Rev. Lett.* **2005**, 95, 267406.
- [19] D. Birkedal, J. Shah, *Phys. Rev. Lett.* **1998**, 81, 2372.
- [20] A. P. Kovács, R. Szipöcs, K. Osvay, Z. Bor, *Opt. Lett.* **1995**, 20, 788.
- [21] D. Meshulach, D. Yelin, Y. Silberberg, *J. Opt. Soc. Am. B* **1997**, 14, 2095.
- [22] A. P. Kovács, K. Osvay, G. Kurdi, M. Görbe, J. Klebniczki, Z. Bor, *Appl. Phys. B: Lasers Opt.* **2005**, 80, 165.
- [23] P. Bowlan, P. Gabolde, A. Shreenath, K. McGresham, R. Trebino, S. Akturk, *Opt. Express* **2006**, 14, 11892.
- [24] P. Bowlan, P. Gabolde, R. Trebino, *Opt. Express* **2007**, 15, 10219.
- [25] P. Bowlan, U. Fuchs, R. Trebino, U. D. Zeitner, *Opt. Express* **2008**, 16, 13663.
- [26] H. Valtna-Lukner, P. Bowlan, M. Löhmus, P. Piksarv, R. Trebino, P. Saari, *Opt. Express* **2009**, 17, 14948.
- [27] J. Cohen, P. Bowlan, V. Chauhan, R. Trebino, *Opt. Express* **2010**, 18, 6583.
- [28] Z. Guang, M. Rhodes, M. Davis, R. Trebino, *J. Opt. Soc. Am. B* **2014**, 31, 2736.
- [29] A. Borzsönyi, A. Kovacs, K. Osvay, *Appl. Sci.* **2013**, 3, 515.
- [30] A. Börzsönyi, A. P. Kovács, M. Görbe, K. Osvay, *Opt. Commun.* **2008**, 281, 3051.
- [31] K. O'Brien, N. D. Lanzillotti-Kimura, H. Suchowski, B. Kante, Y. Park, X. Yin, X. Zhang, *Opt. Lett.* **2012**, 37, 4089.
- [32] S. D. Gennaro, Y. Sonnefraud, N. Verellen, P. Van Dorpe, V. V. Moshchalkov, S. A. Maier, R. F. Oulton, *Nat. Commun.* **2014**, 5, 3748.
- [33] A. J. Ollanik, G. Z. Hartfield, Y. Ji, J. T. Robertson, K. Islam, M. D. Escarra, *Adv. Opt. Mater.* **2019**, 7, 1901128.
- [34] D. R. Smith, D. C. Vier, T. Koschny, C. M. Soukoulis, *Phys. Rev. E: Stat., Nonlinear, Soft Matter Phys.* **2005**, 71, 36617.
- [35] S. Arslanagić, T. V. Hansen, N. A. Mortensen, A. H. Gregersen, O. Sigmund, R. W. Ziolkowski, O. Breinbjerg, *IEEE Antennas Propag. Mag.* **2013**, 55, 91.
- [36] Z. Szabó, G. H. Park, R. Hedge, E. P. Li, *IEEE Trans. Microwave Theory Tech.* **2010**, 58, 2646.
- [37] V. G. Kravets, A. V. Kabashin, W. L. Barnes, A. N. Grigorenko, *Chem. Rev.* **2018**, 118, 5912.
- [38] L. Michaeli, S. Keren-Zur, O. Avayu, H. Suchowski, T. Ellenbogen, *Phys. Rev. Lett.* **2017**, 118, 243904.
- [39] SCHOTT Zemax catalog, [https://refractiveindex.info/download/data/2017/schott\\_2017-01-20b.agf](https://refractiveindex.info/download/data/2017/schott_2017-01-20b.agf) (accessed: May 2020).
- [40] A. Berkhout, A. F. Koenderink, *ACS Photonics* **2019**, 6, 2917.
- [41] L. Michaeli, H. Suchowski, T. Ellenbogen, *Laser Photonics Rev.* **2020**, 14, 1900204.
- [42] I. C. Khoo, *Phys. Rep.* **2009**, 471, 221.
- [43] J. Li, S. Gauza, S. T. Wu, *J. Appl. Phys.* **2004**, 96, 19.
- [44] M. C. Fischer, J. W. Wilson, F. E. Robles, W. S. Warren, *Rev. Sci. Instrum.* **2016**, 87, 031101.
- [45] K. Almarzouk, *Appl. Opt.* **1983**, 22, 1893.